Acta Crystallographica Section A
Foundations of Crystallography
ISSN 0108-7673

Received 16 October 2001
Accepted 11 December 2001

Whole powder pattern modelling

P. Scardi* and M. Leoni

Dipartimento di Ingegneria dei Materiali, Università di Trento, 38050 Mesiano (TN), Italy.
Correspondence e-mail: paolo.scardi@ing.unitn.it

A new approach for the modelling of diffraction patterns without using analytical profile functions is described and tested on ball milled f.c.c. Ni powder samples. The proposed whole powder pattern modelling (WPPM) procedure allows a one-step refinement of microstructure parameters by a direct modelling of the experimental pattern. Lattice parameter and defect content, expressed as dislocation density, outer cut-off radius, contrast factor, twin and deformation fault probabilities), can be refined together with the parameters (mean and variance) of a grain-size distribution. Different models for lattice distortions and domain size and shape can be tested to simulate or model diffraction data for systems as different as plastically deformed metals or finely dispersed crystalline powders. TEM pictures support the conclusions obtained by WPPM and confirm the validity of the proposed procedure.

1. Introduction

Recent developments in the field of powder diffraction address the problem of integrating different algorithms in a unique analytical procedure for the study of polycrystalline materials. Structural information, texture (Rietveld, 1969; Popa, 1992; Järvinen, 1999), domain size and lattice defect models (Delhez *et al.*, 1993; Wu *et al.*, 1998; Scardi & Leoni, 1999; Scardi *et al.*, 2000) can all be combined into commonly used Rietveld refinement codes (Kern & Coelho, 1998; Larson & Von Dreele, 1994; Bergmann *et al.*, 2000). Further information concerning phase percentages (Hill, 1993; Madsen *et al.*, 2001) or residual stress and elastic constants can also be included (Howard & Kisi, 1999; Popa, 2000).

In this context, a distinction is usually made between two approaches: structure (Rietveld) refinement, where the integrated intensity is related to a structural model (including *e.g.* atomic positions and occupancy, thermal factors, lattice parameters) and whole powder pattern fitting (WPPF),[1] where structural information is absent or is limited to lattice parameters, typically used to constrain peak positions according to the material's lattice.

Despite the two approaches being devised and used for different applications, the only recognizable difference is in the meaning of peak intensity, simply treated as a fitting parameter in WPPF. Lattice parameters can be refined by both methods [in this case, WPPF is sometimes called the Pawley method (Pawley, 1981; Toraya, 1993)]. Peak positions, written as the reciprocal of interplanar spacings (d^*_{hkl}), can be expressed by Bragg's law, $d^*_{hkl} = 2\sin\theta_{hkl}/\lambda$, which in terms of reciprocal-space vectors ($\mathbf{b}_1$, $\mathbf{b}_2$, $\mathbf{b}_3$) and Miller indices (hkl) provides the following general expression (Langford & Louër, 1982):

$$d^{*2}_{hkl} = h^2\mathbf{b}_1\cdot\mathbf{b}_1 + k^2\mathbf{b}_2\cdot\mathbf{b}_2 + l^2\mathbf{b}_3\cdot\mathbf{b}_3 + 2hk\mathbf{b}_1\cdot\mathbf{b}_2 + 2kl\mathbf{b}_2\cdot\mathbf{b}_3 + 2lh\mathbf{b}_3\cdot\mathbf{b}_1. \quad (1)$$

Equation (1) can be used in a Rietveld or in a WPPF minimization algorithm to refine the values of ($\mathbf{b}_1$, $\mathbf{b}_2$, $\mathbf{b}_3$) (or of the lattice parameters).

The common root of the two methods is the modelling of the entire powder diffraction pattern (or at least a large portion of it) by means of analytical peak-profile functions and suitable polynomials as background (Young, 1993). In this way, it is implicitly accepted that structural and microstructural models are not directly compared with the experimental evidence – the diffraction pattern – but only through the best fit of peak profile functions. Refinable parameters related to structure and microstructure are therefore obtained from peak profile parameters, as refined by a suitable minimization algorithm based on non-linear least squares or, more recently, Bayesian – maximum-entropy methods (Gilmore, 1996). This approach can be easily implemented in computer programs and run on inexpensive and easily available PCs.

However, irrespective of their flexibility and performance, analytical profile functions introduce arbitrary elements in the modelling whose effect cannot be evaluated *a priori*. Diffraction peak profiles, in fact, depend on a complex combination of physical and instrumental effects, which do not necessarily lead to profile shapes that can be modelled by an arbitrary bell-shaped function.

Constraints imposed by the choice of a given analytical function can introduce systematic (model) errors and correlation between structural and non-structural parameters. As a consequence, the results of Rietveld refinement and WPPF

[1] Pattern fitting without structural constraints is generally referred to as pattern decomposition (Langford & Louër, 1996).

can be biased in a rather unpredictable way and their reliability can be difficult to assess.

As a matter of fact, problems arising from the arbitrariness of using analytical profile functions have been mostly neglected so far. Speed and easy computation are main reasons for this choice, even to the expense of reliability of the results.

In this work, we review some recent developments that led to the concept of whole powder pattern modelling (WPPM) (Scardi *et al.*, 2000, 2001*a*,*b*). Experimental data, including intensity data points with their statistical errors, are compared with models based on well defined physical parameters, directly related with those microstructural features responsible for the shape and width of diffraction profiles. WPPM, as compared with WPPF, does not employ arbitrary analytical profile functions. Domain size effects can be described in terms of crystallite shape and size distribution, also considering the presence of planar defects, whereas lattice distortions can be interpreted according to a suitable microstrain model, for instance involving the presence of dislocations. The proposed approach can be integrated in a Rietveld algorithm, *i.e.* explicitly include the structural information.

In the present work, we apply the method to the case of f.c.c. materials and crystalline grains with spherical shape. From a conceptual point of view, however, the extension to different symmetries and to crystalline domains with different shapes is straightforward (Scardi & Leoni, 2001). To illustrate the application of WPPM to the study of real materials, we considered a series of heavily deformed metal samples obtained by ball milling (b.m.). Mechanisms of grain refinement and lattice defects generation are discussed in the light of the results provided by WPPM and transmission electron microscopy (TEM).

2. Theoretical basis

2.1. Diffracted intensity from a defected material

Peak profiles observed in powder diffraction patterns result from different contributions: an instrumental profile component (g), usually including instrument-related geometrical factors (*e.g.* diffraction optics and flat sample in Bragg–Brentano geometry) and sample transparency, and a sample profile component (f), due to the microstructure of the studied material. The convolution of the profile components ($h = g \otimes f$) yields the observed experimental peak profile (Klug & Alexander, 1974). In the present work, we explicitly consider the contribution from the specimen microstructure, all the other components being included in the instrumental profile (IP), which can be determined experimentally by means of suitable profile standards [*e.g.* NIST SRM 660*a* (Cline *et al.*, 2000; Leoni *et al.*, 1998)] or modelled, *e.g.* by a fundamental parameters approach (FPA) (Cheary & Coelho, 1992).

As a further general assumption, we consider polycrystalline samples devoid of preferred orientations and macrostrain (applied, thermal or residual), with coherent diffraction domains (crystallites) sufficiently small to provide appropriate counting statistics (Klug & Alexander, 1974). The last condition is easily fulfilled by highly dispersed metal or ceramic powders, or by defected materials with submicrometre crystallites, to which the method proposed in this work is addressed.

Basic expressions for the diffracted intensity hold independently of the symmetry of the crystal lattice; however, the specific algorithm described in this work is valid for f.c.c. materials. An extension to other crystal structures, in principle, should not present major conceptual difficulties and will be the object of future developments.

The diffraction profile is conveniently described in terms of the diffraction vector ($\mathbf{d}^*$) in the reciprocal lattice, whose modulus is $d^* = 2\sin\theta/\lambda$, where θ is the diffraction angle and λ the X-ray wavelength. For cubic materials, in the absence of lattice defects and load or residual strain, the diffraction vector in the Bragg condition is $d^*_{\{hkl\}}$ ($d^*_{\{hkl\}} = 2\sin\theta_{\{hkl\}}/\lambda$), where the Miller indices are reported in curly brackets, since we refer to the family of planes as a whole. As we will see in the following, it is important to make a distinction between $d^*_{\{hkl\}}$ and d^*_{hkl}, the value of the diffraction vector for a specific combination of *hkl*, which is related to a subcomponent of the observed profile.

The intensity from a set of {*hkl*} planes can be written as the sum of the contributions from all the *hkl* profile subcomponents:

$$I_{\{hkl\}}(d^*, d^*_{\{hkl\}}) = k(d^*) \sum_{hkl} w_{hkl} I_{hkl}(d^* - d^*_{\{hkl\}} - \delta_{hkl}), \qquad (2)$$

where $k(d^*)$ includes microstructure-independent terms (*e.g.* Lorentz–polarization (Lp), $|F|^2$ *etc.*), which are constant or known functions of d^*.[2] w_{hkl} is a weight function for the *hkl* component and δ_{hkl} is a shift from the reciprocal-space point corresponding to the Bragg condition in the absence of defects and strain. Both w_{hkl} and δ_{hkl} depend on the specific defects present in the material: explicit expressions for twin and deformation faults are given in §2.2.3. The contribution of a given subcomponent can be written as

$$I_{hkl}(s_{hkl}) = \int_{-\infty}^{\infty} T^{\mathrm{IP}}(L) \langle \exp[2\pi i \psi(L)] \rangle \langle \exp[2\pi i \varphi(L)] \rangle \times \exp[2\pi i L s_{hkl}] \, \mathrm{d}L, \qquad (3)$$

where $T^{\mathrm{IP}}(L)$ is the Fourier Transform (FT) of the IP and the two terms in brackets ($\langle\,\rangle$) are average phase factors due to lattice distortions (ψ) and crystallite size/faulting (φ), respectively. In this way, we are implicitly assuming that there is no interaction between linear and planar defects (separate averages). The integration variable, L (a length in real space), is inversely proportional to $d^*_{\{hkl\}}$ and is the conjugate variable of $s_{hkl} = d^* - (d^*_{\{hkl\}} + \delta_{hkl})$, the distance from the peak centroid in the reciprocal space.

[2] Actually, $k(d^*)$ includes absorption and may also account for other effects, *e.g.* extinction, which depend on sample density, that strictly speaking should be considered as a microstructural feature.

The explicit form of each term in (3) and rules for the summation in (2) will be discussed in the next sections, under the following assumptions:

(i) Crystalline domains are spherical. Therefore, broadening due to size effects is isotropic, *i.e.* independent of (*hkl*). The system of spheres considered is polydisperse, diameters being distributed according to a given distribution function. Possible choices considered in this work include a lognormal distribution, which seems appropriate to several real cases including highly deformed metals (Valiev *et al.*, 1994; Islamgaliev *et al.*, 1997; Valiev *et al.*, 2000) or finely dispersed powders (Granqvist & Buhrman, 1976; Kiss *et al.*, 1999; Krill & Birringer, 1998; Langford *et al.*, 2000), a Γ distribution or a distribution resulting from grain growth phenomena, recently introduced by York (1999). Other distribution functions can easily be introduced. Different crystallite shapes can also be considered (Scardi & Leoni, 2001), even if non-spherical shapes involve a more or less marked anisotropy in size-broadening effects. In this case, assumptions on the orientation of the crystal axes with respect to the crystallite are required.

(ii) Lattice distortions have the same effect on all profile subcomponents for a given {*hkl*} family. Formally, we can write $\varepsilon_{hkl}(L) = \varepsilon_{\{hkl\}}(L)$. We further assume dislocations as source for lattice distortions; in this context, the above hypothesis requires all dislocation slip systems to be equally populated. Different lattice distortion sources can also be considered as briefly discussed in the following.

(iii) Faulting planes belong to the {111} family; however, faults in each crystalline grain are present on a given crystallographic plane only, say (111). The effect of stacking faults is calculated according to Warren's theory (Warren, 1969) suitably extended and corrected for higher faulting probabilities (Velterop *et al.*, 2000).

2.2. Line-broadening components

2.2.1. Instrumental profile (IP) component. The instrumental profile is assumed symmetrical across the measurement angular range, a condition easily obtained by a suitable choice of slits and other optical components [like monochromators or analyser crystals (Leoni *et al.*, 1998)]. $T^{\rm IP}(L)$ is the cosine FT of an analytical function representing the IP like, *e.g.* Voigt (*V*) or pseudo-Voigt (pV) curves (Langford, 1992; Leoni *et al.*, 1998). If we consider a pV, the explicit form of $T^{\rm IP}(L)$ is

$$T^{\rm IP}_{\rm pV}(L) = (1-k)\exp(-\pi^2\sigma^2L^2/\ln 2) + k\exp(-2\pi\sigma L), \quad (4)$$

where $\sigma = \omega\cos\theta/\lambda$; σ and ω are the half-width at half-maximum (HWHM) in the reciprocal and 2θ space, respectively. k can be written in terms of the pV mixing parameter, η (Scardi & Leoni, 1999):

$$k = [1 + (\varphi_C/\varphi_G)(1-\eta)/\eta]^{-1} = [1 + (\pi\ln 2)^{-1/2}(1-\eta)/\eta]^{-1}, \quad (5)$$

where we have introduced the shape factors (φ = 2HWHM/β) of the Gaussian (*G*) and Lorentzian (*C*) components, respectively: $\varphi_G = 2[(\ln 2)/\pi]^{1/2} = 0.93949$, $\varphi_C = (2/\pi) = 0.63662$ (Langford, 1992).

The trends of IP width and shape can easily be parameterized in order to produce an analytical description of the IP and its FT for any required d^* (Scardi & Leoni, 1999). This can be performed by fitting pV functions to the experimental profiles of a line-profile powder standard (NIST SRM 660*a*; Cline *et al.*, 2000) and then by modelling the $\omega(\theta)$ and the $\eta(\theta)$ trends with suitable empirical polynomials [*e.g.* Caglioti expression for $\omega(\theta)$ and a parabola for the mixing factor (Langford, 1987; Scardi & Leoni, 1999)].

A fundamental parameters approach (Cheary & Coelho, 1992; Kern & Coelho, 1998) can be used as an alternative to synthesize the IP from physical and geometrical parameters of the instrument/sample system. Suitable expression can be worked out and used in (3) in place of $T^{\rm IP}_{\rm pV}(L)$.

It is also possible to consider an asymmetric instrumental profile. In this case, $T^{\rm IP}_{\rm pV}(L)$ should be substituted by a complex FT, *i.e.* an additional sine term should be introduced. We will not consider this case in detail here, but the relevant extension to the proposed method is straightforward.

2.2.2. Lattice distortions. The average phase factor introduced by lattice distortions, $\langle\exp[2\pi i\psi(Ld^*_{\{hkl\}}, \varepsilon_{\{hkl\}}(L))]\rangle$, depends on a microstrain $[\varepsilon_{\{hkl\}}(L)]$ related to the lattice distortion on a coherence distance *L*. Different mechanisms like dislocations (Krivoglaz & Ryaboshapka, 1963; Wilkens, 1970*a*,*b*), inclusions in a crystalline matrix (van Berkum, 1994) or surface relaxation in nanoscale powders (Nunes & Lin, 1995; Leoni & Scardi, 2001) can be a source of lattice distortions, leading to different expressions for $\varepsilon_{\{hkl\}}(L)$. The strain effect can also be anisotropic, *i.e.* line broadening can depend on {*hkl*} in a non-monotonic way with respect to d^*. Otherwise, a fluctuation of lattice parameter a from grain to grain (for instance, a fluctuation in chemical composition) can be the origin of an effective strain, $\varepsilon = (a - a_o)/a_o$, where a_o is the average lattice parameter; in this case, ε is isotropic and independent of *L*.

According to Warren (1969), the average phase factor for distortions can be written as

$$\begin{aligned}&\langle\exp[2\pi i\psi(Ld^*_{\{hkl\}}, \varepsilon_{\{hkl\}}(L))]\rangle \\ &\quad = \langle\cos[2\pi Ld^*_{\{hkl\}}\varepsilon_{\{hkl\}}(L)]\rangle + i\langle\sin[2\pi Ld^*_{\{hkl\}}\varepsilon_{\{hkl\}}(L)]\rangle \\ &\quad = A^D_{\{hkl\}}(L) + iB^D_{\{hkl\}}(L). \end{aligned} \quad (6)$$

It is useful to consider the power expansion of the two average trigonometric terms in (6):

$$\begin{aligned} A^D_{\{hkl\}}(L) &= 1 - 2\pi^2L^2d^{*2}_{\{hkl\}}\langle\varepsilon^2_{\{hkl\}}(L)\rangle \\ &\quad + \tfrac{2}{3}\pi^4L^4d^{*4}_{\{hkl\}}\langle\varepsilon^4_{\{hkl\}}(L)\rangle - O(Ld^*_{\{hkl\}})^6 \quad (7a) \\ B^D_{\{hkl\}}(L) &= -\tfrac{4}{3}\pi^3L^3d^{*3}_{\{hkl\}}\langle\varepsilon^3_{\{hkl\}}(L)\rangle + O(Ld^*_{\{hkl\}})^5. \quad (7b) \end{aligned}$$

From (7), we can see that the information required to model lattice distortion effects concerns the moments $[\langle\varepsilon^n_{\{hkl\}}(L)\rangle]$ of the microstrain distribution (Warren, 1969; van Berkum 1994). The well known Warren–Averbach method (Warren, 1969)

considers terms up to $(Ld^*_{\{hkl\}})^2$ and $B^D_{\{hkl\}}(L) = 0$. The last condition is strictly valid if the microstrain distribution function, $p(\varepsilon_{\{hkl\}}(L))$, from which moments are calculated (van Berkum, 1994), is an even function. However, as the imaginary part goes with $(Ld^*_{\{hkl\}})^3$, $B^D_{\{hkl\}}(L)$ is frequently neglected.

If we assume that lattice distortions are due to dislocations, according to Wilkens's approach (Wilkens, 1970*a*,*b*), the real term can be written as

$$A^D_{\{hkl\}}(L) = \exp[-\tfrac{1}{2}\pi b^2 \overline{C}_{hkl} \rho d^{*2}_{\{hkl\}} L^2 f^*(L/R_e)], \qquad (8)$$

where **b** is the Burgers vector with $b = a_o/2^{1/2}$ for the $\{111\}\langle 110\rangle$ slip system in f.c.c. materials, and f^* is given by (van Berkum, 1994)

$$f^*(x) \cong \begin{cases} -\ln x + \dfrac{7}{4} - \ln 2 + \dfrac{x^2}{6} - \dfrac{32x^3}{225\pi} & \text{for } x \le 1 \\ \dfrac{256}{45\pi x} - \left(\dfrac{11}{24} + \dfrac{\ln 2x}{4}\right)x^{-2} & \text{for } x > 1. \end{cases} \qquad (9)$$

Other expressions have been proposed to model the effect of dislocations: essentially they are all based on a leading term of the type $\exp[-(Ld^*_{\{hkl\}})^2 \ln(R/L)]$ [where R is the outer cut-off radius or an equivalent parameter (Krivoglaz *et al.*, 1983; Groma *et al.*, 1988; van Berkum, 1994)] in (8) that diverges for large L. Since conventional methods are used only in the limit of small L, usually this is not considered a serious limitation. The expressions for (8) available from the literature always involve approximations; however, an important point concerning (9) is that it does not diverge for large L values, an important condition in (3), since we need an expression valid for any L to model profiles without introducing spurious oscillations. However, the validity of the $\exp[-(Ld^*_{\{hkl\}})^2 \ln(R/L)]$ functional form has been demonstrated for different arrangements and types of dislocations (Kamminga & Delhez, 2000), so the applicability of (8) is rather general.

It is also possible to add higher-order terms to the exponent in (8). The leading term is of the type $(Ld^*_{\{hkl\}})^4 g(L/R)\rho^2 \overline{C}^2_{hkl}$, where $g(L/R)$ is given by Wilkens (1970*b*). This term, whose weight in the expression for $A^D_{\{hkl\}}(L)$ is considerably lower than that of the $L^2 f^*(L/R_e)$ term, is significant only for high values of the product $(Ld^*_{\{hkl\}})$, *i.e.* for high diffraction angles and around the peak top, where large L values are important.

$\overline{C}_{hkl}$ is the average contrast factor, which accounts for the anisotropic line-broadening effect of the dislocation strain field. Actually, according to the different dislocation models, part of the dependence on (hkl) is carried by R_e (Klimanek & Kužel, 1988); however, this dependence should be much weaker than that of $\overline{C}_{hkl}$ (Klimanek & Kužel, 1988; Kužel & Klimanek, 1989), and in the present work R_e is considered as a fitting parameter independent of (hkl). As originally proposed by Stokes & Wilson (1944), line-broadening anisotropy can be introduced by assuming a linear dependence of the microstrain on the orientational parameter H. Consequently, the average contrast factor for cubic systems can be written as

$$\overline{C}_{hkl} = \overline{C}_{h00}(1 + qH) = \overline{C}_{h00}\left[1 + q\frac{h^2k^2 + h^2l^2 + k^2l^2}{(h^2 + k^2 + l^2)^2}\right]. \qquad (10)$$

If the elastic constants of the material (c_{ij} or s_{ij}) are known, $\overline{C}_{h00}$ and q can be obtained for different types of dislocations (Wilkens, 1987). In addition, as recently shown by Ungár *et al.* (1999), $\overline{C}_{h00}$ and q for screw and edge dislocations in cubic systems can be conveniently expressed in a parametric form of the elastic constants. In this way, we can assume that $A^D_{\{hkl\}}(L)$ depends on ρ and R_e only; additionally, q can be refined in order to adjust the modelling for the appropriate screw/edge character of the dislocation system present in the specific sample under study.

Expressions analogous to (10) can be written for materials with different symmetry. In fact, the functional form of the dependence of the contrast factor on *hkl* is solely determined by symmetry considerations. In particular, contrast factors can be related to Laue-group invariants whose expressions are available from the literature (Popa, 1998; Stephens, 1999). The case of hexagonal materials has been discussed in detail by Klimanek & Kužel (Klimanek & Kužel, 1988; Kužel & Klimanek, 1989).

2.2.3. Faulting. The average phase term due to size/faulting (SF) effects, $\langle \exp[2\pi i\varphi(L; d^*_{\{hkl\}}, L_0/h_0^2)]\rangle$ can also be written as

$$\langle \exp[2\pi i\varphi(L; d^*_{\{hkl\}}, L_0/h_0^2)]\rangle = A^{\rm SF}_{hkl}(D) + iB^{\rm SF}_{hkl}(D). \qquad (11)$$

According to our hypotheses (*cf.* §2.1),

$$A^{\rm SF}_{hkl}(L) = A^S(L)A^F_{hkl}(L) \qquad (12a)$$

$$B^{SF}_{hkl}(L) = A^S(L)A^F_{hkl}(L)B^F_{hkl}(L), \qquad (12b)$$

where the $A^S(L)$ and $A^F_{hkl}(L)$ are cosine terms for crystallite size (*size*) and faulting, respectively, whereas $B^F_{hkl}(L)$ is the sine term due to faulting.

Since twin and deformation faults are assumed to be present in (111) planes only, line broadening (as well as asymmetry and peak shift from Bragg position) shows a characteristic (hkl) dependence that is contained in the expressions for $A^F_{hkl}(L)$ and $B^F_{hkl}(L)$ (Velterop *et al.*, 2000):

$$A^F_{hkl}(L) = (1 - 3\alpha - 2\beta + 3\alpha^2)^{|(1/2)Ld^*_{\{hkl\}}(L_o/h_o^2)\sigma_{L_o}|} \qquad (13a)$$

$$B^F_{hkl}(L) = -\sigma_{L_o}\frac{L}{|L|}\frac{L_o}{|L_o|}\frac{\beta}{(3 - 12\alpha - 6\beta + 12\alpha^2 - \beta^2)^{1/2}}, \qquad (13b)$$

where α and β are, respectively, the deformation and twin fault probabilities, $L_o = h + k + l$, $h_o^2 = h^2 + k^2 + l^2$ and

$$\sigma_{L_o} = \begin{cases} +1 & \text{for } L_o = 3N + 1 \\ 0 & \text{for } L_o = 3N \\ -1 & \text{for } L_o = 3N - 1 \end{cases} \qquad N = 0, \pm1, \pm2, \ldots. \qquad (14)$$

Equations (13*a*) and (13*b*) differ from those developed by Warren [*cf.* equation (13.62) in Warren (1969)] in that we considered the sign of L, consistently with the use of L instead of $|L|$ in the argument of the sine term of the FT (see below).

The (hkl)-dependent shift of the diffraction peak centroid (in reciprocal space) due to faulting is[3]

$$\delta_{hkl} = \left\{\frac{1}{2\pi}\arctan\left[\frac{(3-12\alpha-6\beta+12\alpha^2-\beta^2)^{1/2}}{(1-\beta)}\right]-\frac{1}{6}\right\} \times d^*_{\{hkl\}}(L_o/h_o^2)\sigma_{L_o}. \quad (15)$$

The expressions above indicate that the contribution of faulting to line broadening and peak position is anisotropic and depends on α and β.

Equations (13) and (15) involve a different effect of faulting for the various profile subcomponents. Profile width, asymmetry and peak-position shift are determined by α, β *and* by L_o, σ_{L_o}.

Depending on the specific combination of Miller indices, up to four different profile subcomponents are present in cubic systems. This can be responsible for a complex shape of the observed {hkl} diffraction peak (Velterop *et al.*, 2000), which is not simply broadened and shifted as assumed by the conventional WA method.

The summation over the different profile subcomponents in (2) is therefore determined by the rules of faulting. In the most general case, the sum is over the multiplicity (m) of a reflection, but considerations above suggest that it is not necessary to sum up all the m subcomponents. The summation is extended to permutations of the L_o sign, which are responsible for the subcomponent profiles. Each of them has a different weight, w_{hkl} in (2), depending on the number of subcomponents with the same faulting effects [*e.g.* refer to Table 2 of Velterop *et al.* (2000)].

2.2.4. Crystallite size. No physical principle can be invoked *a priori* to assess grain morphology because crystallite size is not a tensor property of the system (Nye, 1987; Scardi & Leoni, 2001); as a consequence, it is necessary to formulate some model of crystallite shape. Size distribution is also an issue, since it is unlikely that crystalline grains in real systems have equal size.

According to a spherical crystallite model, *size* effects give a FT component [$A^S(L)$] independent of (hkl). In addition, we assume that diameters (D) are dispersed according to a suitable distribution function. In principle, one can use any distribution function appropriate to the specific case of study, but for simplicity in the following we consider three examples of two-parameter distributions.

A lognormal distribution is defined as (Lloyd, 1984)

$$g_l(D) = \frac{1}{D\omega(2\pi)^{1/2}}\exp\left[-\frac{(\ln D-\gamma)^2}{2\omega^2}\right], \quad (16a)$$

where ω^2 and γ are lognormal variance and lognormal mean. Distribution moments are given by $M_{l,n} = \exp[n\gamma + (n^2/2)\omega]$, consequently, the mean of the distribution (first moment) is $M_{l,1} = \exp(\gamma + \frac{1}{2}\omega^2)$ and the variance is $M_{l,2} - (M_{l,1})^2 = \exp(2\gamma+\omega^2)[\exp(\omega^2)-1]$.

A possible alternative to the lognormal is the Γ distribution:[4]

$$g_g(D) = \frac{\nu}{M_{g,1}\Gamma(\nu)}\left(\frac{\nu D}{M_{g,1}}\right)^{\nu-1}\exp(-\nu D/M_{g,1}), \quad (16b)$$

where $M_{g,1}$ is the mean size and ν is the ratio between the square of the mean size and the variance: $\nu = M_{g,1}^2/(M_{g,2}-M_{g,1}^2)$ ($\nu \geq 1$). $M_{g,i}$ is the ith moment of the distribution. The Γ distribution is quite flexible, ranging from an exponential when $\nu = 1$ to a Gaussian for increasing ν.

A valuable alternative when normal growth phenomena are considered is the distribution proposed by York (1999), which, after normalization, reads

$$g_y(D) = \frac{1}{\mu\Gamma(\sigma)}\left(\frac{\sigma D}{\mu}\right)^{\sigma}\exp(-\sigma D/\mu), \quad (16c)$$

whose mean and variance are $M_{y,1} = \mu(1+\sigma)/\sigma$ and $M_{y,1}\mu/\sigma$, respectively.

The *size* FT, $A^S(L)$, for a system of spheres can be calculated as proposed by Scardi *et al.* (2000, 2001*a*) and by Scardi & Leoni (2001). We start from the FT of the intensity scattered by a spherical crystal (Wilson, 1962):

$$A_c(L,D) = 1 - \frac{3|L|}{2D} + \frac{|L|^3}{2D^3}. \quad (17)$$

Then the FT of the system of spheres is given by (Scardi & Leoni, 2001)

$$A^S(L) = \frac{\int_L^\infty A_c(L,D)D^3 g(D)\,\mathrm{d}D}{\int_0^\infty D^3 g(D)\,\mathrm{d}D}. \quad (18)$$

By using one of the $g(D)$ [equations (16*a*)–(16*c*)] in the above equation, we can write expressions for the FT for a system of spheres whose diameters are dispersed according to the given distribution. The FTs for a lognormal, Γ or York distribution are, respectively,[5]

$$A_l^S(L) = \sum_{n=0}^{3} H_n^c \frac{M_{l,3-n}}{2M_{l,3}}\,\mathrm{erfc}\left[\frac{\ln(K^cL)-\gamma-(3-n)\omega^2}{\omega\times 2^{1/2}}\right]L^n \quad (19a)$$

$$A_g^S(L) = \sum_{n=0}^{3} H_n^c\left(\frac{\nu}{M_{g,1}}\right)^n \frac{\Gamma(\nu+(3-n),(K^cL\nu/M_{g,1}))}{\Gamma(\nu+3)}L^n \quad (19b)$$

$$A_y^S(L) = \sum_{n=0}^{3} H_n^c\left(\frac{\sigma}{\mu}\right)^n \frac{\Gamma(\sigma+(4-n),(K^cL\sigma/\mu))}{\Gamma(\sigma+4)}L^n. \quad (19c)$$

For spherical crystals, $K^c = 1$, $H_0^c = 1$, $H_1^c = -3/2$, $H_2^c = 0$, $H_1^c = 1/2$ (Scardi & Leoni, 2001).

If necessary, different crystal shapes can be considered but this introduces an hkl dependence in the FT. As shown recently by Scardi & Leoni (2001), the functional form of

[3] It can be demonstrated that, in the limit of low probabilities, (15) can be written as in the original form proposed by Warren: $\delta_{hkl} = (3^{1/2}/4\pi)\alpha d^*_{\{hkl\}}(L_o/h_o^2)\sigma_{L_o}$. Warren's expressions for $A^F_{hkl}(L)$ and $B^F_{hkl}(L)$ can be obtained from (13), by dropping α^2 and β^2 terms.

[4] Also referred to as Poisson distribution in a previous paper (Scardi & Leoni, 2001). However, the name Γ is more appropriate and widely used for this kind of continuous distribution and will be used throughout this paper.

[5] The incomplete Γ function is defined as $\Gamma(x,a) = \int_a^\infty y^{x-1}\exp(-y)\,\mathrm{d}y$, whereas $\Gamma(x) = \Gamma(x,0)$.

(19*a*)–(19*c*) holds as far as polyhedra or spheres are considered. K^c and H_n^c coefficients for several common solids are reported in the above cited paper.

2.3. Explicit expression for equation (3)

Equation (3) can be written in terms of sine and cosine components of the FT related to the various sources of broadening. If we consider (6), (8), (11), (13) and (19*a*) [or (19*b*)], the most general expression is

$$I_{hkl}(s_{hkl}) = \int_{-\infty}^{\infty} T_{\rm pV}^{\rm IP} A^S A_{hkl}^F \{[A_{\{hkl\}}^D - B_{\{hkl\}}^D B_{hkl}^F]\cos(2\pi L s_{hkl}) - [A_{\{hkl\}}^D B_{hkl}^F - B_{\{hkl\}}^D]\sin(2\pi L s_{hkl})\}\,{\rm d}L, \quad (20)$$

where for simplicity the dependence on L has been omitted. In the assumption that $B_{\{hkl\}}^D \cong 0$ (*cf.* §2.2.2), the expression above reduces to

$$I_{hkl}(s_{hkl}) = \int_{-\infty}^{\infty} T_{\rm pV}^{\rm IP} A^S A_{hkl}^F A_{\{hkl\}}^D [\cos(2\pi L s_{hkl}) - B_{hkl}^F \sin(2\pi L s_{hkl})]\,{\rm d}L. \quad (21)$$

There are essentially two approaches to the use of (2) and (21):

(*a*) adopt an analytical function (*e.g.* a Voigtian) to fit the experimental profiles; suitable conditions can be written to connect profile parameters (Gaussian and Lorentzian widths in the case of a Voigtian profile function) to the IP and *size–microstrain* parameters; this is the basis of WPPF, as described in recent work by Scardi *et al.* (Scardi & Leoni, 1999; Scardi *et al.*, 2000, 2001*a*,*b*);

(*b*) use (2) to directly model experimental profiles; for each {*hkl*} reflection, *hkl* subcomponent profiles can be modelled by means of (21) (Scardi *et al.*, 2001*a*,*b*).

Approach (*b*) should be distinguished from (*a*) and WPPF in general, irrespective of results being similar or not, and should be referred to as whole powder pattern modelling (WPPM). In principle, (*b*) should be preferable, since it does not introduce unnecessary artefacts and errors due to the arbitrary choice of an analytical profile function, as in (*a*). As a drawback, owing to the convolution integral in (21), WPPM requires lengthy calculation. Therefore, approach (*a*) can be easier to implement in existing Rietveld algorithms, since it involves conditions on parameters of the adopted analytical profile function. Simulations have shown that (*a*) can provide results in reasonable agreement with those obtained by (*b*). Additional details and examples of applications of WPPF can be found elsewhere (Scardi *et al.*, 2000, 2001*a*,*b*).

In the following, we will focus on WPPM. According to this approach, (2) can be used to model experimental data to directly refine size/faulting and lattice distortion parameters within a non-linear least-squares (NLSQ) routine. The WPPM algorithm was written in Fortran (Compaq Visual Fortran, Version 6.6) and uses the MINPACK library (Garbow *et al.*, 1996) implementation of the Levenberg–Marquardt method for the NLSQ. Convergence is usually reached in few iterations (less than 10). With a 1 GHz PC, a complete refinement for a typical f.c.c. phase (7–8 reflections) takes less than 3 h. Speed can be considerably increased if a few preliminary iterations are performed by WPPF.

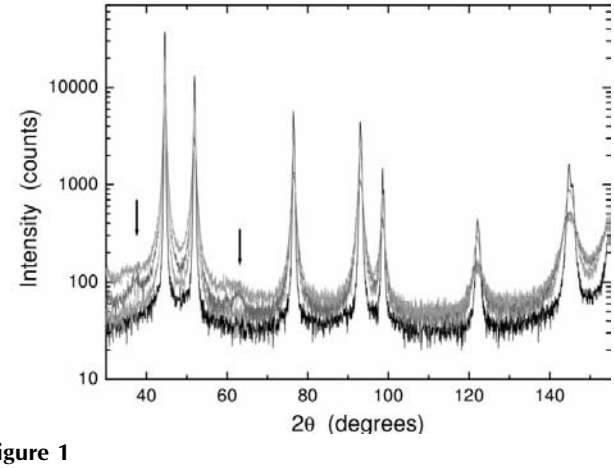

Figure 1
XRD patterns of nickel powder. From lowest curve: as received and after 12 h, 48 h and 96 h ball milling. Arrows mark the positions of NiO main reflections.

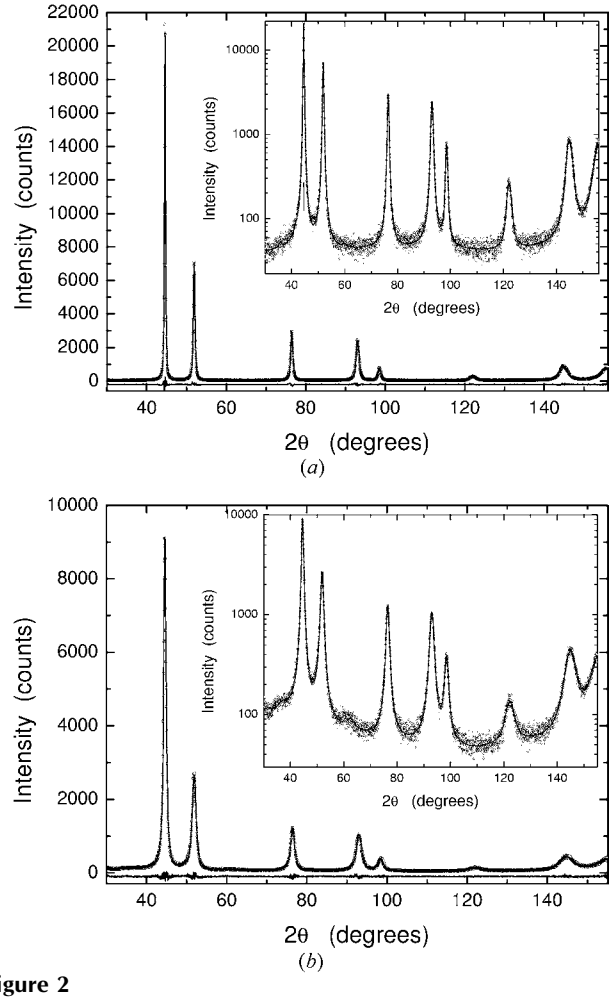

Figure 2
Whole powder pattern modelling of ball-milled Ni samples: (*a*) 12 h and (*b*) 96 h.

3. Experimental

Ni powder samples (Johnson–Matthey, 99.9% purity) were milled in a Fritsch Pulverisette 7 planetary micromill (agate grinding bowl and 5 zirconia balls). The same amount of powder (2.5 g) was milled in static air for different times: 6 h, 12 h, 24 h, 48 h and 96 h. The powder-to-ball ratio was 7.5. XRD patterns were collected on a Rigaku PMG-VH powder diffractometer operated at 40 kV and 45 mA (Cu tube). Goniometer set-up, including narrow slits (1/2° divergence, 2° incident beam Soller, 2° diffracted beam Soller, 0.15 mm receiving) and a graphite curved-crystal diffracted-beam analyser, provided narrow and symmetrical instrumental profiles over the required angular range (Leoni *et al.*, 1998). High definition of background and peak tails was achieved by long counting times (60 s per 0.05° 2θ step). TEM pictures were collected by a 300 kV Philips CM30 microscope equipped with a Gatan 794 multiscan CCD camera.

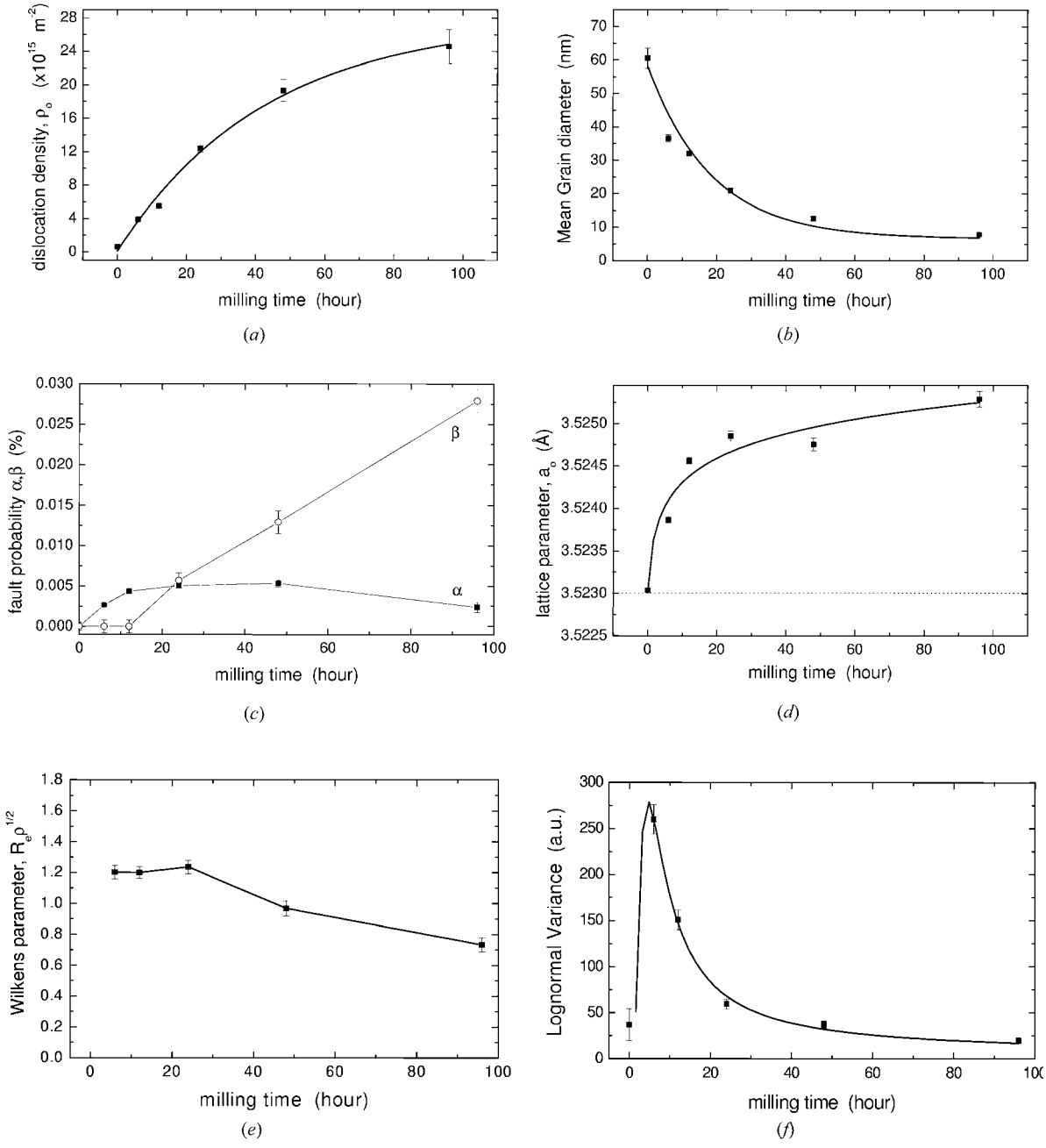

Figure 3
WPPM results as a function of the ball-milling time: (*a*) dislocation density, (*b*) mean grain diameter, (*c*) twin (β) and deformation (α) faults , (*d*) lattice parameter (dotted line indicates bulk Ni value), (*e*) Wilkens parameter ($R_e\rho^{1/2}$), (*f*) variance of lognormal size distribution.

4. Results and discussion

4.1. Application of WPPM to ball-milled nickel powder

Ball milling is known to produce severe plastic deformations in metallic powders, leading to extremely high defect densities and a fine dispersion of crystalline domains (Salimon *et al.*, 1999; Valiev *et al.*, 2000; Zhao *et al.*, 2001). WPPM can provide detailed information on the nature and density of lattice defects and, in general, on the evolution of the microstructure. Fig. 1 shows the XRD patterns of some of the ball-milled Ni powder samples (as received, 12 h, 48 h and 96 h). The effect of mechanical treatment on line profiles is clearly visible, as well as the anisotropic nature of the line broadening. It is also worth noting that, despite the presence of few reflections, on a sufficiently resolved scale (*e.g.* in a log scale plot) peak overlapping is always present, even for short b.m. times and in the as-received sample. This feature is a clear indication that single-peak analysis is inappropriate, in this as well as in many other real cases of study. Peak-profile overlapping in powder patterns is present as a rule more than as an exception, and *a priori* background subtraction and peak-profile separation can be a risky procedure. Consequently, conventional methods always involve a certain (undetermined) level of unreliability.

Weak reflections, additional to those of the Ni phase, are observed in the tails of the lower-angle peaks in Fig. 1. The weak lines are produced by a minor amount of NiO, formed during the ball milling. Owing to the possible effect on the pattern modelling, NiO (f.c.c.) reflections were included in the WPPM together with the main-phase Ni peaks.

The quality of the WPPM can be appreciated in Fig. 2, where the experimental and modelled patterns are shown for two different b.m. times. WPPM results, in terms of evolution of grain size and lattice defects parameters as a function of b.m. time, are shown in Fig. 3. The main results can be summarized as follows.

(i) Dislocation density (Fig. 3*a*) increases with b.m. time, but the rate tends to decrease with time.

(ii) Grain size, in terms of mean grain diameter (Fig. 3*b*), decreases with time, with a trend somewhat opposite to that found for the dislocation density.

(iii) Deformation faults (Fig. 3*c*) are produced in a low amount (well below 1%).

(iv) Twin faults (Fig. 3*c*) are absent for short times; longer b.m. leads to a progressive increase of twin faults, up to $\sim 3\%$ after 96 h.

(v) Lattice parameter (Fig. 3*d*) follows a trend similar to that of the dislocation density, rapidly increasing in the early stages of b.m., and then saturating after 24–48h.

The initial b.m. stage, when considerable plastic deformation occurs, leads to a rapid increase of dislocation density; for longer time, the value tends to saturate. Even if the trend is relatively smooth and continuous, microstructure evolution is a more complex process because the arrangement and interaction between dislocations evolves with b.m. time (Fecht *et al.*, 1990; Salimon *et al.*, 1999). Evidence can be found in the Wilkens parameters (Wilkens, 1970*a*) $M = R_e\rho^{1/2}$, decreasing (below unity) for prolonged b.m. (Fig. 3*e*). This can indicate an increase in dislocation interaction with b.m. time, which is compatible with a progressive evolution from a dislocation-cell structure to a fully nanocrystalline state, with formation of non-equilibrium grain boundaries made of high density of extrinsic dislocations.

Grain-size information also supports this picture. Grain reduction, in fact, tends to stop after $\sim$48 h, little grain size refinement being achieved afterwards. Similar results have been obtained for most f.c.c. metals (Salimon *et al.*, 1999; Tian & Atzmon, 1999; Valiev *et al.*, 2000). Here WPPM analysis provides further information concerning the effect of b.m. because, in addition to the mean grain diameter (Fig. 3*b*), we can follow the evolution of the grain-size distribution with time, as shown in Fig. 4.

Grain size in the as-received sample is evenly dispersed about the average value of 60 nm, with a nearly symmetrical distribution, characterized by a moderate dispersion. This feature can also be appreciated in Fig. 3(*f*), where the variance of the lognormal distribution is reported as a function of the b.m. time. Ball milling initially leads to a widening and simultaneous shift of the distribution to lower diameters. This is the stage (0–12 h) where b.m. reaches the highest efficiency in introducing lattice defects, with strong plastic deformation. After 12–24h, while the grain-size reduction effect tends to saturate, the distribution narrows again, the variance reducing accordingly. Extensive b.m., therefore, progressively eliminates large grains (above *ca* 40 nm), whose fraction is drastically reduced after 24 h. Beyond this treatment time, b.m. slowly leads to a shift of the size distribution to small diameter values, the variance tending to decrease. After 48–96 h, grain diameter saturates to $\sim$8 nm, with a low dispersion about the mean value, and a properly nanocrystalline state is reached.

Deformation faults (Fig. 3*c*) are produced in a low amount during b.m. (well below 1%). This is probably justified by the high stacking-fault energy (SFE) of pure Ni (200 mJ m^{-2}) (Salimon *et al.*, 1999). However, impurities can play a key role in reducing the SFE and oxygen incorporation is very likely, given the presence of NiO. Stacking faults are typically produced by plastic deformation and dislocation motion in

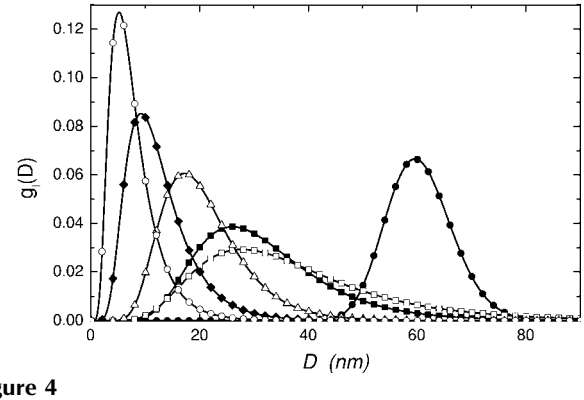

Figure 4
Grain diameter distributions for Ni powders: as received (black circle), after 6 h (white square), 12 h (black square), 24 h (white triangle), 48 h (black diamond) and 96 h (white circle) of ball milling.

f.c.c. materials, therefore α is not expected to increase sensibly with b.m. time, since dislocation motion is progressively hindered and virtually absent in nanocrystals (Sanders *et al.*, 1995).

Twin faults, on the contrary, are absent in the early b.m. stages but progressively increase with time. The formation of twins is probably the result of a general tendency to reduce surface energy in the finely dispersed microstructure produced by extensive b.m. Similar evidence has been obtained in previous studies (Sanders *et al.*, 1995; Chatterjee & Sen Gupta, 2001).

The trend of the lattice parameter – rapidly increasing with time and then saturating – has already been observed in ball-milled metals (Salimon *et al.*, 1999; Valiev *et al.*, 2000; Zhao *et al.*, 2001) and attributed to different phenomena induced by the plastic deformation. Supersaturation of vacancies has been reported in evaporated thin films (Liu *et al.*, 1994) as a result of a general increase in solubility in finely dispersed grains. In fact, according to the Gibbs–Thomson equation, vacancy and defect solubility is expected to increase as D^{-1} (Liu *et al.*, 1994). In our case, the presence of NiO traces supports the hypothesis of a considerable oxygen incorporation in the Ni matrix, to the point that excess oxygen forms oxide (Salimon *et al.*, 1999). Given the evolution of the grain-size distribution, however, we cannot expect a simple hyperbolic trend of the lattice parameter as a function of the average grain size. An additional effect is related to the high elastic strains produced by a high density of extrinsic dislocations at grain boundaries. As shown by Nazarov *et al.* (1996), the presence of disordered arrays of extrinsic dislocations and disclinations forming grain boundaries leads to a lattice expansion that can be estimated from the values of dislocation density and grain size [$\Delta V/V \propto b^2\rho\ln(D/b)$]. However, values calculated from the present results are below the observed lattice expansion [*e.g.*, for the sample ball milled 96 h, compare the measured expansion $\Delta V/V \approx 19\,(3) \times 10^{-4}$ with the value calculated from the Nazarov *et al.* (1996) formulae, $\Delta V/V \approx 8 \times 10^{-4}$], therefore it is reasonable to conclude that high elastic strains produced by non-equilibrium grain boundaries and increased oxygen solubility both contribute to the increase of lattice parameter with the b.m. time.

We can therefore conclude that ball milling increases lattice defects as expected but the trend is rather peculiar. After ~24 h, b.m. tends to lose efficiency in introducing lattice damage and the trends of dislocation density, mean grain diameter, lattice parameter and deformation fault probability tend to flatten out. Correspondingly, twin faults appear and their probability increases with the b.m. time. In this way, the high deformation energy, partly stored in the microstructure, tends to be released by the formation of low-energy boundaries. This is in agreement with the conclusion of Fecht *et al.* (1990) that prolonged milling leads to disappearance of the dislocation cells and a subsequent appearance of a properly nanocrystalline state.

4.2. TEM evidence and comparison with WPPM data

Transmission electron microscopy can provide a direct insight into the nanocrystalline state of b.m. materials (Valiev *et al.*, 2000), which is especially important to integrate and validate the WPPM results described so far.

A limit in the TEM analysis of b.m. materials is defect density. Dislocations densities above ~10^{15} m^{-2} cannot be quantitatively evaluated. Moreover, it can be difficult and somewhat subjective to single out crystalline domains in grains with a dislocation-cell structure (Ungár *et al.*, 2001), typical of the early stages of b.m., or when grains have dimensions comparable or bigger than the TEM sample under study. For these reasons, the analysis of crystalline grains can be better performed in the nanocrystalline phase, *i.e.* for long b.m. times. As shown in Fig. 5, after 96 h nanocrystalline domains are clearly visible and sufficiently delineated to permit a quantitative analysis. Since grains are reasonably equiaxial and smaller than the thickness of the TEM sample, the observed grain size is likely to be very close to the true size with no need for stereological corrections. Average grain sizes were

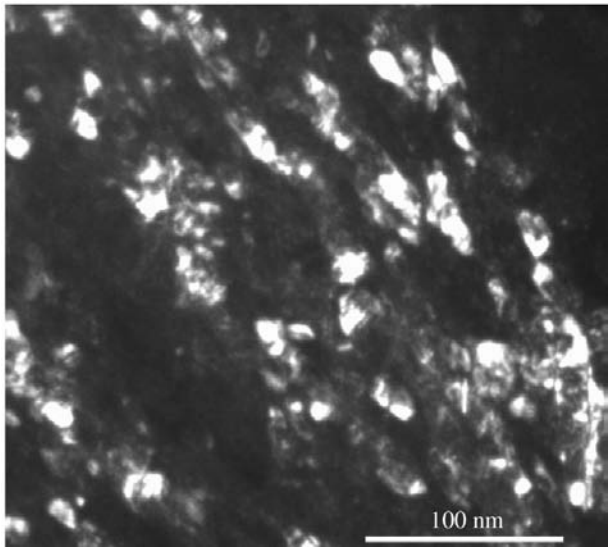

Figure 5
Dark-field TEM picture of sample 96 h.

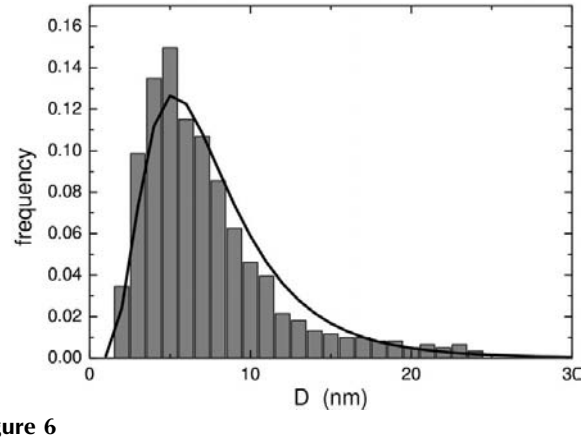

Figure 6
Grain-size distribution for sample 96 h: TEM (histogram) and WPPM result (line).

obtained as equivalent-circle diameters (Krill & Birringer, 1998) [$D_e = 2(A/\pi)^{1/2}$, where A is the projected area] from several dark-field pictures like that of Fig. 5. Fig. 6 shows the TEM size distribution resulting from nearly 850 grains for the sample ball milled for 96 h (histogram), together with the corresponding result obtained by WPPM (line) (reported from Fig. 4). The agreement is quite good, considering that the two techniques are affected by different experimental errors and in any case provide size measurements under completely different principles. Looking at the fine details in Fig. 6, we see that the TEM distribution is not exactly a lognormal, and most disagreement concerns size 10–15 nm. Here we should note that faulting is treated differently in the two analyses. The WPPM analysis includes the contribution of faulting: grain size is an overall size of crystalline domains (including defects). TEM, instead, can show the presence of twins (most likely, twinned grains do not appear simultaneously in the same dark-field picture because of the different orientation of the lattice planes), whereas the resolution of our dark-field pictures is not sufficient to disclose stacking (deformation) faults by TEM (Krill & Birringer, 1998). These differences between XRD analysis and TEM imaging of planar defects can contribute to the discrepancy between the distributions of Fig. 6: in fact, given the percentage of twin faults (∼3%), we expect several large grains to be crossed by the planar defect so that they appear smaller in a dark-field picture.

The presence of twins has already been reported in other studies on nanocrystalline metals obtained by plastic deformation (Sanders *et al.*, 1995; Chatterjee & Sen Gupta, 2001). In our samples, direct evidence was provided by high-resolution TEM (Fig. 7) that shows a twinned grain in the 96 h sample. This observation confirms the WPPM results, showing the tendency to form low-energy boundaries after prolonged ball milling, to reduce the excess energy mostly stored in the grain boundaries.

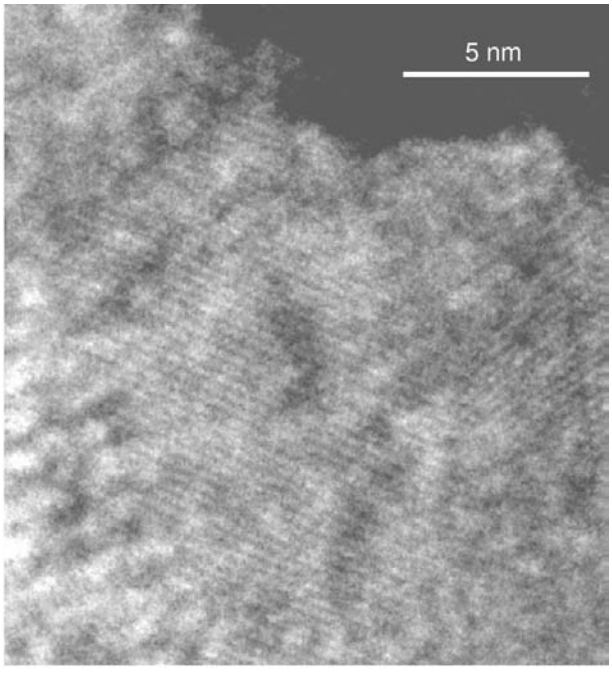

Figure 7
HREM picture for the Ni sample ball-milled for 96 h.

5. Conclusions

Whole powder pattern modelling can be regarded as a new paradigm for the refinement of diffraction data, based on physical models of material microstructure, without using analytical functions for profile fitting. The proposed approach was tested on a series of ball-milled f.c.c. Ni powder samples, whose features were described in detail by WPPM. TEM data support the conclusions drawn on the basis of WPPM results, showing a remarkable agreement between grain-size distributions obtained by the two techniques for a nanocrystalline Ni sample obtained by extensive ball milling.

As an important distinction with respect to most conventional line-profile methods, physical parameters refined by WPPM are obtained by a direct comparison with the experimental pattern, so that the correct counting statistics are used with no additional (*a priori* unknown) systematic error components typical of analytical profile fitting. Virtually any line-broadening component – instrumental or physical (sample related) – can be included in the modelling. Even if the procedure in its present formulation applies to cubic (f.c.c.) materials, an extension to different symmetries is relatively straightforward and will be the object of future studies.

WPPM can also be regarded as a direct and unbiased way to test different models (*e.g.* see contributions to Snyder *et al.*, 1999; van Berkum, 1994) of lattice-defect (point, line, plane) broadening and to simulate powder patterns. For instance, in addition (or as an alternative) to the dislocation model shown in this work, specific expressions for other lattice distortion sources can be introduced in the WPPM [*e.g.* misfitting inclusions, compositional fluctuations, grain surface relaxation (Leoni & Scardi, 2001)].

Different domain shape or domain distributions can be directly tested, and corresponding results compared. The general approach does not change if the size-broadening component is replaced, for instance according to the model recently proposed by Armstrong *et al.* (2001), based on a maximum-entropy approach.

As such, WPPM can be proposed as a new paradigm for the analysis of powder diffraction data, to be used as an analytical tool in materials science studies or to be included in a Rietveld refinement to get rid of the arbitrariness in the use of analytical profiles.

The authors are particularly grateful to C. Tosi (University of Trento, Italy) and A. Migliori (CNR-LAMEL, Bologna, Italy) for TEM sample preparation and pictures and to S. Setti (University of Trento, Italy) for assistance in XRD measurements.

References

Armstrong, N., Cline, J. P., Kalceff, W. & Bonevich, J. (2001). *Proceedings of the 3rd Conference on Accuracy in Powder Diffraction*, edited by J. P. Cline, J. Post & P. Scardi. Abstract 22-25.4.2001, NIST, Gaithersburg, MD, USA.

Bergmann, J., Kleeberg, R., Haase, A. & Breidenstein, B. (2000). *Mater. Sci. Forum*, **347–349**, 303–308.

Berkum, J. G. M. van (1994). PhD thesis, Delft University of Technology, The Netherlands.

Chatterjee, P. & Sen Gupta, S. P. (2001). *Philos. Mag.* A**81**, 49–60.

Cheary, R. W. & Coelho, A. A. (1992). *J. Appl. Cryst.* **25**, 109–120.

Cline, J. P., Deslattes, R. D., Staudenmann, J.-L., Kessler, E. G., Hudson, L. T., Henins, A. & Cheary, R. W. (2000). Certificate SRM 660a, NIST, Gaithersburg, MD, USA.

Delhez, R., de Keijser, Th. H., Langford, J. I., Louër, D., Mittemeijer E. J. & Sonneveld, E. J. (1993). *The Rietveld Method*, edited by R. A. Young, pp. 132–166. Oxford University Press.

Fecht, H. J., Hellstern, E., Fu, Z. & Johnson, W. L. (1990). *Metall. Trans.* A**21**, 2333–2339.

Garbow, B. S., Hillstrom, K. E. & More, J. J. (1996). MINPACK Project. Argonne National Laboratory, November 1996 (http://www.netlib.org/minpack).

Gilmore, C. J. (1996). *Acta Cryst.* A**52**, 561–589.

Granqvist, C. G. & Buhrman, R. A. (1976). *J. Appl. Phys.* **47**, 2200–2205.

Groma, I., Ungar, T. & Wilkens, M. (1988). *J. Appl. Cryst.* **21**, 47–53.

Hill, R. (1993). *The Rietveld Method*, edited by R. A. Young, pp. 61–101. Oxford University Press.

Howard, C. J. & Kisi, E. H. (1999). *J. Appl. Cryst.* **32**, 624–633.

Islamgaliev, R. K., Chmelik, F. & Kuzel, R. (1997). *Mater. Sci. Eng.* A**237**, 43–51.

Järvinen, M. (1999). *Defect and Microstructure Analysis by Diffraction*, edited by R. L. Snyder, J. Fiala & H.-J. Bunge, pp. 556–559. Oxford University Press.

Kamminga, J.-D. & Delhez, R. (2000). *J. Appl. Cryst.* **33**, 1122–1127.

Kern, A. A. & Coelho, A. A. (1998). *A New Fundamental Parameters Approach in Profile Analysis of Powder Data.* New Delhi: Allied Publishers Ltd. ISBN 81-7023-881-1.

Kiss, L. B., Süderlund, J., Nikhsson, G. A. & Granqvist, C. G. (1999). *Nanostruct. Mater.* **12**, 327–332.

Klimanek, P. & Kužel, R. Jr (1988). *J. Appl. Cryst.* **21**, 59–66.

Klug, H. P. & Alexander, L. E. (1974). *X-ray Diffraction Procedures for Polycrystalline and Amorphous Materials*, 2nd ed. New York: Wiley.

Krill, C. E. & Birringer, R. (1998). *Philos. Mag.* **77**, 621–640.

Krivoglaz, M. A., Martynenko, O. V. & Ryaboshapka, K. P. (1983). *Phys. Met. Metall.* **55**, 1–12.

Krivoglaz, M. A. & Ryaboshapka, K. P. (1963). *Fiz. Metall.* **15**, 18–28.

Kužel, R. Jr & Klimanek, P. (1989). *J. Appl. Cryst.* **22**, 299–307.

Langford, J. I. (1987). *Prog. Cryst. Growth Charact.* **14**, 185–211.

Langford, J. I. (1992). *Accuracy in Powder Diffraction II*, in *NIST Spec. Publ.* No. 846, edited by E. Prince & J. K. Stalick, pp. 110–126. Gaithersburg, MA: US Department of Commerce.

Langford, J. I. & Louër, D. (1982). *J. Appl. Cryst.* **15**, 20–26.

Langford, J. I. & Louër, D. (1996). *Rep. Prog. Phys.* **59**, 131–234.

Langford, J. I., Louër, D. & Scardi, P. (2000). *J. Appl. Cryst.* **33**, 964–974.

Larson, A. C. & Von Dreele, R. B. (1994). *General Structure Analysis System (GSAS)*. Report LAUR 86-748, Los Alamos National Laboratory, NM, USA.

Leoni, M. & Scardi, P. (2001). *Proceedings of Size–Strain III*, edited by P. Scardi & E. J. Mittemejier, pp. 31–32. University of Trento, Italy. ISBN 88-8443-014-3.

Leoni, M., Scardi, P. & Langford, J. I. (1998). *Powder Diffr.* **13**, 210–215.

Liu, X. D., Zhang, H. Y., Lu, K. & Hu, Z. Q. (1994). *J. Phys. Condens. Matter*, **6**, L497–L502.

Lloyd, E. (1984). *Handbook of Applicable Mathematics*, Vol. 4, *Statistics.* Chichester: Wiley.

Madsen, I. C., Scarlett, N. V. Y., Cranswick, L. M. D. & Lwin, T. (2001). *J. Appl. Cryst.* **34**, 409–426.

Nazarov, A. A., Romanov, A. E. & Valiev, R. Z. (1996). *Scr. Mater.* **34**, 729–734.

Nunes, A. C. & Lin, D. (1995). *J. Appl. Cryst.* **28**, 274–278.

Nye, J. F. (1987). *Physical Properties of Crystals: their Representation by Tensors and Matrices*, reprint edition. Oxford University Press.

Pawley, G. S. (1981). *J. Appl. Cryst.* **14**, 357–361.

Popa, N. C. (1992). *J. Appl. Cryst.* **25**, 611–616.

Popa, N. C. (1998). *J. Appl. Cryst.* **31**, 176–180.

Popa, N. C. (2000). *J. Appl. Cryst.* **33**, 103–107.

Rietveld, H. M. (1969). *J. Appl. Cryst.* **2**, 65–71.

Salimon, A. I., Korsunky, A. M. & Ivanov, A. N. (1999). *Mater. Sci. Eng.* A**271**, 196–205.

Sanders, P. G., Witney, A. B., Weertman, J. R., Valiev, R. Z. & Siegel, R. W. (1995). *Mater. Sci. Eng.* A**204**, 7–11.

Scardi, P. & Leoni, M. (1999). *J. Appl. Cryst.* **32**, 671–682.

Scardi, P. & Leoni, M. (2001). *Acta Cryst.* A**57**, 604–613.

Scardi, P., Leoni, M. & Dong, Y. H. (2000). *Eur. Phys. J.* B**18**, 23–30.

Scardi, P., Leoni, M. & Dong, Y. H. (2001*a*). *Mater. Sci. Forum*, **378–381**, 132–139.

Scardi, P., Leoni, M. & Dong, Y. H. (2001*b*). *CPD Newsletter*, **24**, 23–24.

Snyder, R. L., Fiala, J. & Bunge, H.-J. (1999). Editors. *Defect and Microstructure Analysis by Diffraction.* Oxford University Press.

Stephens, P. W. (1999). *J. Appl. Cryst.* **32**, 281–289.

Stokes, A. R. & Wilson, A. J. C. (1944). *Proc. Cambridge Phys. Soc.* **40**, 197–198.

Tian, H. H. & Atzmon, M. (1999). *Acta Mater.* **47**, 1255–1261.

Toraya, H. (1993). *The Rietveld Method*, edited by R. A. Young, pp. 254–275. Oxford University Press.

Ungár, T., Dragomir, I., Révész, Á. & Borbély, A. (1999). *J. Appl. Cryst.* **32**, 992–999.

Ungár, T., Gubicza, J., Ribárik, G. & Borbély, A. (2001). *J. Appl. Cryst.* **34**, 298–310.

Valiev, R. Z., Islamgaliev, R. K. & Alexandrov, I. V. (2000). *Prog. Mater. Sci.* **45**, 103–189.

Valiev, R. Z., Kozlov, E. V., Ivanov, Y. F., Lian, J., Nazarov, A. A. & Baudelet, B. (1994). *Acta Metall. Mater.* **42**, 2467–2474.

Velterop, L., Delhez, R., de Keijser, Th. H., Mittemeijer, E. J. & Reefman, D. (2000). *J. Appl. Cryst.* **33**, 296–306.

Warren, B. E. (1969). *X-ray Diffraction.* Reading, MA: Addison–Wesley.

Wilkens, M. (1970*a*). *Phys. Status Solidi A*, **2**, 359–370.

Wilkens, M. (1970*b*). *Fundamental Aspects of Dislocation Theory*, Vol. II, edited by J. A. Simmons, R. de Wit & R. Bullough, pp. 1195–1221. *Natl Bur. Stand. (US) Spec. Publ.* No. 317. Washington, DC: NBS.

Wilkens, M. (1987). *Phys. Status Solidi A*, **104**, K1–K6.

Wilson, A. J. C. (1962). *X-ray Optics*, 2nd ed. London: Methuen.

Wu, E., Mac, E., Gray, A. & Kisi, E. H. (1998). *J. Appl. Cryst.* **31**, 356–362.

York, B. R. (1999). *Adv. X-ray Anal.* **41**, 544–555.

Young, R. A. (1993). Editor. *The Rietveld Method.* Oxford University Press.

Zhao, Y. H., Sheng, H. W. & Lu, K. (2001). *Acta Mater.* **49**, 365–375.